Solution-processed inorganic perovskite crystals as achromatic quarter-wave plates

Xiaomei Chen [1], Wen-gao Lu [1,2], Jialun Tang[1], Yongyou Zhang [3 ✉], Yongtian Wang [2], Gregory D. Scholes [4] and Haizheng Zhong [1 ✉]

Waveplates are widely used in photonics to control the polarization of light[1,2]. Often, they are fabricated from birefringent crystals that have different refractive indices along and normal to the crystal axis. Similar optical components are found in the natural world, including the eyes of mantis shrimp[3,4] and the iridescence of giant clams[5], fish[6] and plants[7]. Optical retardation in biology relies on sophisticated self-assembly, whereas man-made systems comprise multiple-layered materials[8–11]. Here we report a discovery that bridges these two design principles. We observe wideband achromatic retardation in the visible and near-infrared (532–800 nm) regions for Cs_4PbBr_6 perovskite crystals embedded with $CsPbBr_3$ nanocrystals. We explain our observations as matched dispersions of the refractive indices of the ordinary and extraordinary rays caused by the ordered embedding of the nanocrystals in the host. The wideband performance and ease of fabrication of these perovskite materials are attractive for future applications.

Optical anisotropy of a birefringent crystal can split the incident light into two beams, labelled the ordinary ray (o-ray) and the extraordinary ray (e-ray)[12], in the process of optical retardation (Fig. 1a). Introducing a suitable delay between these two rays produces the quarter-wave (QW) effect, which is typically achievable only for a narrow wavelength range. The challenge for fabricating a QW plate that is effective over a broad wavelength range is to control the phase delay of each wavelength[13]. Such achromatic retardation in the visible region can be achieved using multiple-layered birefringent crystals. For example, in previous works, achromatic waveplates were fabricated by combining quartz and magnesium fluoride or sapphire to reduce the influence of the phase delay[14,15]. These materials require experienced design and usually need complicated multi-step fabrication processes[16], as summarized in Supplementary Table 1.

Recently, halide perovskite-based crystals have emerged as a new category of optoelectronic materials for the applications of solar cells[17,18], light-emitting diodes[19–21], photodetectors[22], lasing[23] and ferroelectrics[24]. Here we report the surprising discovery that single crystals of Cs_4PbBr_6 show remarkable birefringence. Cs_4PbBr_6 perovskite crystals (for example, sample I below) were grown using a slow-cooling method[25,26]. The pure Cs_4PbBr_6 crystal belongs to the trigonal phase[27], so it shows intrinsic birefringence to tune the polarization of transmitted light. Similar to conventional uniaxial crystals[28,29], the birefringence of a pure Cs_4PbBr_6 crystal shows the usual feature of wavelength-dependent retardation. On the contrary,

we found that when the Cs_4PbBr_6 crystal contains embedded $CsPbBr_3$ nanocrystals (NCs) in the matrix (for example, as in sample II below), the sample displays achromatic retardation, that is, it can modulate the polarization states of transmitted light without any obvious wavelength dependence. Our study finds that the embedded $CsPbBr_3$ NCs in the Cs_4PbBr_6 crystal play an important role in determining the observed unusual achromatic retardation.

The as-grown Cs_4PbBr_6 crystals were polished using silk and polishing powder before optical measurements. Figure 1b presents a photograph of a typical pure Cs_4PbBr_6 single crystal (sample I) with a size of $3.0 \times 3.0 \times 1.3$ mm (see Supplementary Fig. 1a) grown from an aqueous solution[26]. It is noted that sample I has a parallelepiped shape with good transparency. As shown in Fig. 1c, the Cs_4PbBr_6 crystal with embedded $CsPbBr_3$ NCs (sample II) has a yellow-green colour with a size of $5.0 \times 5.0 \times 1.1$ mm (see Supplementary Fig. 1b). According to the X-ray diffraction patterns in Supplementary Fig. 1c, the front surface of these samples can be assigned to the (024) plane.

The presence of $CsPbBr_3$ NCs in sample II is evidenced by the observed spectroscopic features in the ultraviolet-visible diffuse reflection and photoluminescence spectra (see Supplementary Fig. 2). In our study, this conclusion is also supported by the observation of Tyndall light scattering[30,31] incident from a red 633 nm laser (see Supplementary Fig. 3). The embedded $CsPbBr_3$ NCs in the Cs_4PbBr_6 crystals were further determined by applying high-resolution transmission electron microscope (HRTEM) measurements. Figure 1d shows the HRTEM image of the Cs_4PbBr_6 crystals observed from the (100) direction and the corresponding fast Fourier transform pattern, confirming the crystal structure of Cs_4PbBr_6. As shown in Fig. 1e and Supplementary Fig. 4, the HRTEM images of the embedded $CsPbBr_3$ NCs can be identified by clarifying the lattice distances corresponding to the cubic $CsPbBr_3$ phase, as summarized in Supplementary Table 2. These results provide direct evidence of the incorporation of $CsPbBr_3$ NCs in the Cs_4PbBr_6 crystal host. Based on the detailed analysis of 11 particles, the alignment between the (111) plane of the embedded $CsPbBr_3$ NCs and the (012) plane of Cs_4PbBr_6 is found consistently to be ~18°. Similarly, the alignment between the (111) plane of the embedded $CsPbBr_3$ NCs and the (100) plane of Cs_4PbBr_6 is ~90°. As shown in Supplementary Fig. 5, the embedded $CsPbBr_3$ NCs are ordered and aligned with preferred directions.

Figure 2a shows a schematic of the optical setup used for our birefringence measurements. Linearly polarized 532 nm and 633 nm lasers typically served as the light sources (their polarization

[1]MIIT Key Laboratory for Low-dimensional Quantum Structure and Devices, School of Materials Science & Engineering, Beijing Institute of Technology, Beijing, China. [2]Beijing Engineering Research Center of Mixed Reality and Advanced Display, School of Optics and Photonics, Beijing Institute of Technology, Beijing, China. [3]Beijing Key Laboratory of Nanophotonics and Ultrafine Optoelectronic Systems, School of Physics, Beijing Institute of Technology, Beijing, China. [4]Department of Chemistry, Princeton University, Princeton, NJ, USA. ✉e-mail: yyzhang@bit.edu.cn; hzzhong@bit.edu.cn
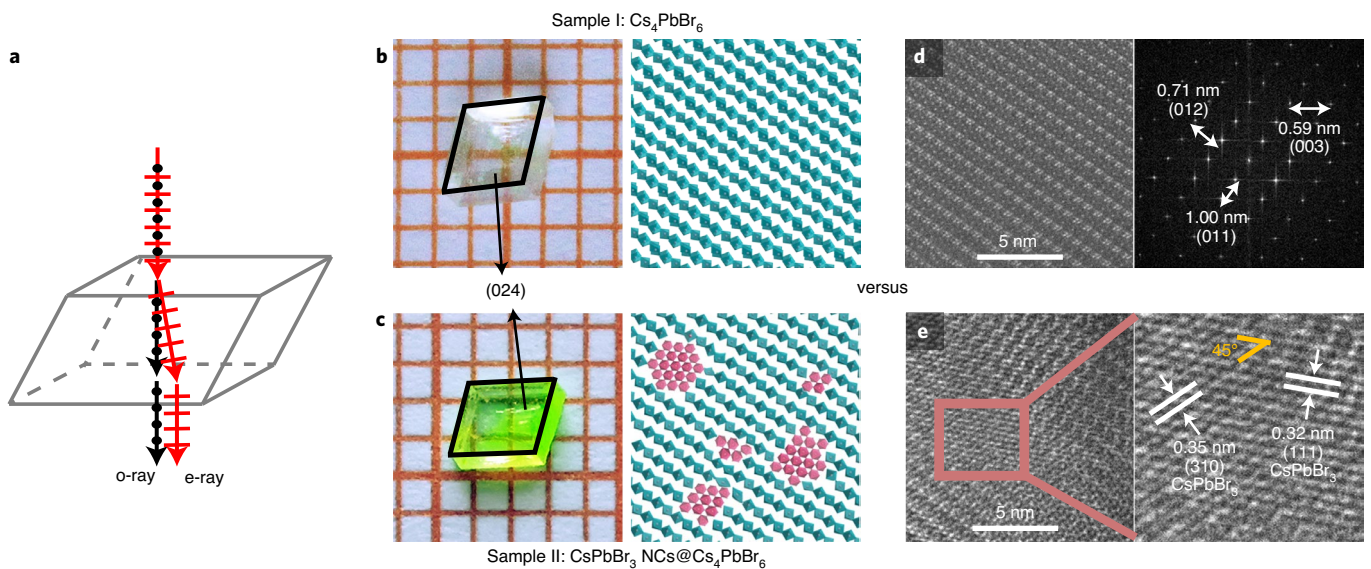
Fig. 1 | Illustration of crystal birefringence and the samples of Cs$_4$PbBr$_6$ crystals without and with embedded CsPbBr$_3$ NCs. a, Schematic illustration of crystal birefringence. **b**, Optical image of pure Cs$_4$PbBr$_6$ crystal and its schematic structure (sample I, blue isolated octahedra represent the lattice). Grid scale, 1mm. **c**, Optical image of the Cs$_4$PbBr$_6$ crystal host with embedded CsPbBr$_3$ NCs and its schematic structure (sample II, pink corner-shared octahedra represent the NCs). Grid scale, 1mm. **d**, HRTEM image of the Cs$_4$PbBr$_6$ crystals observed from the (100) direction and the corresponding fast Fourier transform pattern. **e**, HRTEM images of embedded CsPbBr$_3$ NCs.
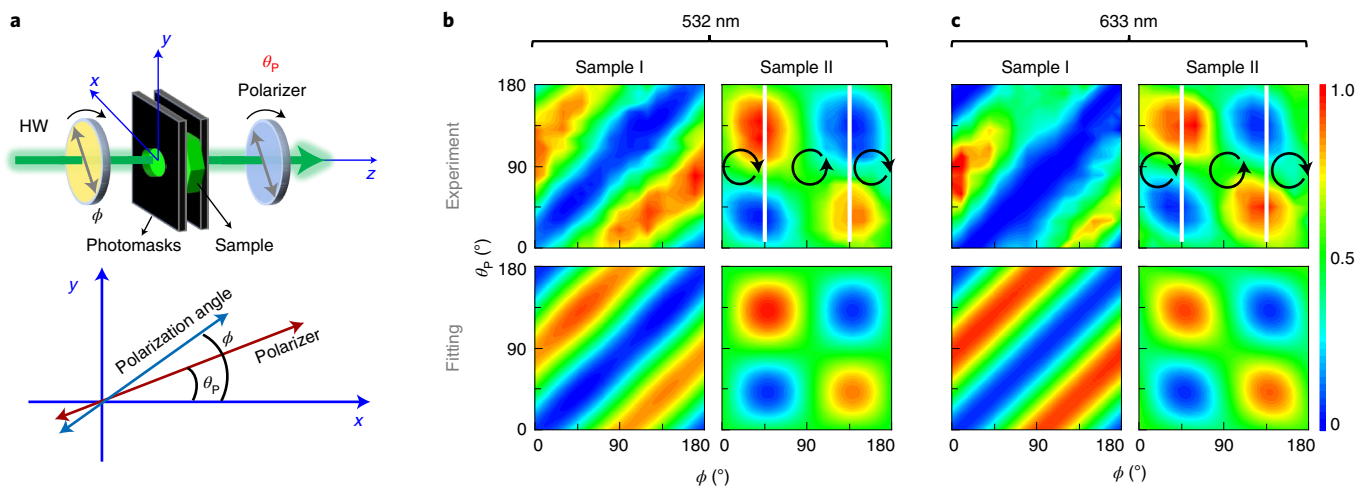

Fig. 2 | The measurement setup and the results of polarization modulation. a, Schematic diagram of the polarization measurement setup (top) and angle arrangement (down). **b,c**, Experimental and fitting intensities of transmitted light for 532 nm laser (**b**) and for 633 nm laser (**c**). The data are normalized to their maximum values, respectively.

properties are shown in Supplementary Fig. 6), but other sources were also used for this study as described below. The incident light was kept perpendicular to the (024) plane of both samples. The polarizations of the incident and transmitted lights were determined using polarizers and their corresponding intensities were recorded using a fibre optic spectrometer. The polarization angle of the incident light after passing through the half-wave (HW) plate is recorded as ϕ and the transmission azimuthal angle of the polarizer is recorded as θ_P (both with respect to the horizontal line).

Figure 2b shows the intensity variations of the transmitted 532 nm light with ϕ and θ_P for samples I and II. For convenience, the samples were fixed during the measurements, while the HW plate was rotated to change the polarization direction of the incident light. Both samples exhibit birefringence properties. Sample I

acts as an HW plate, while sample II behaves as a QW plate. We further investigated the birefringence characteristics with incident light of a 633 nm laser. As shown in Fig. 2c, the polarization distribution for sample I varied with the change in wavelength from 532 nm to 633 nm, indicating wavelength-dependent birefringence. This observation is similar to properties reported previously for inorganic crystals[29].

In contrast to sample I, the variation of the polarization distribution for sample II shows only a slight wavelength dependence, suggesting an achromatic retardation effect. The wavelength independence was further explored by measuring the variation of the polarization distribution with the wavelength using various light sources, including a xenon lamp (see Supplementary Fig. 7) and mono-wavelength light-emitting diodes (see Supplementary
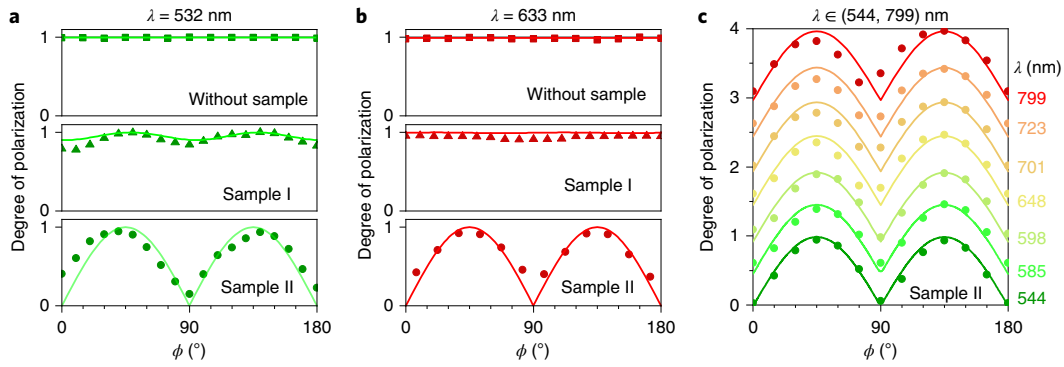
Fig. 3 | The analysis of the degree of polarization measurements with fitting results. a,b, The degree of polarization for the reference, sample I and sample II under laser light of 532 nm (**a**) and 633 nm (**b**). **c**, The degree of polarization of sample II under incident light from light-emitting diodes at 544, 585, 598, 648, 701, 723 and 799 nm. Dots, experiment data; solid lines, fitting results. The data are moved up with a step size of 0.5.

Figs. 8 and 9). As a QW plate, sample II can change the light polarization from linearly polarized to left- or right-hand circularly polarized (see Supplementary Figs. 10 and 11). The polarization of the transmitted light after sample II was determined by the polarization angle of the incident light (ϕ), as shown in Fig. 2b,c, where the polarization of left- or right-hand polarized light is indicated by the circular arrows.

The Cs_4PbBr_6 crystal with embedded $CsPbBr_3$ NCs shows an unusual wavelength-independent QW effect across a broad wavelength band ranging from 532 to 800 nm. We also investigated other materials derived from Cs_4PbBr_6 crystals, for example, a chloride-doped sample containing embedded NCs, which shows cyan-coloured photoluminescence (see Supplementary Fig. 12a). Similarly, achromatic retardation was also found for this sample (see Supplementary Fig. 12b). We therefore conclude that the embedded $CsPbBr_3$ NCs of sample II are the key factor for explaining the wavelength independence of the polarization modulation.

The HRTEM images have shown that the embedded $CsPbBr_3$ NCs have a size between 2–5 nm and that the inter-NC distance is about 10–50 nm. Because these values are much less than the wavelength of visible light, both of the crystals (with and without embedded NCs) can be considered as continuous birefringent dielectric matter for visible light. The key feature of sample II is the ordered aligned $CsPbBr_3$ NCs in the host crystal. Therefore, we applied the birefringent theory to compare light transport in these two kinds of crystal. Provided that normal incident linearly polarized light takes the polarization state ($\cos(\phi),\sin(\phi),0$) with the polarization angle ϕ (Fig. 2a), the transmission coefficients for the x- and y-polarized components can be modelled as follows:

$$t_x = \frac{2n_o}{2n_o \cos(n_o kd) - i(1 + n_o^2)\sin(n_o kd)}\cos(\phi), \quad (1)$$

$$t_y = \frac{2n_\gamma}{2n_\gamma \cos(n_\gamma kd) - i(1 + n_\gamma^2)\sin(n_\gamma kd)}\sin(\phi), \quad (2)$$

where the xy plane coincides with the (024) facet of the two samples. The parameters k and d are the light wavevector and the sample thickness, respectively; n_o and n_e represent the refractive indices for the o-ray and the e-ray, respectively. In addition, n_γ is defined as

$$n_\gamma = n_o n_e / \sqrt{(1 - \cos^2\gamma)n_o^2 + n_e^2\cos^2\gamma},$$

with γ being the direction angle of the optical axis with respect to the z axis, as described in the fitting section in the Supplementary

Information. The intensity of the transmitted light is proportional to $|t_x|^2 + |t_y|^2$. For the x- and y-polarized components, the phase shifts of samples I and II can be fitted using equations (1) and (2). For example, the phase shifts of the x- and y-polarized lights for sample I are about -0.39π and 0.74π under the 532 nm laser, respectively, while the values for sample II are about -0.12π and 0.38π, respectively.

Figure 2b,c shows the comparison between the fitting and experimental results. The good agreement provides an effective strategy to derive the variation of refractive index with wavelength in which n_o and n_e are taken as the two fitted parameters, as described in the fitting section in the Supplementary Information. We then applied this measurement to determine the refractive index of a $LiNbO_3$ crystal. The refractive indices of the ordinary and extraordinary light rays of $LiNbO_3$ crystal, derived from the data of Supplementary Figs. 13 and 14, are well fitted with the reported value with a deviation of less than 1% (refs. [32,33]). The refractive indices of ordinary and extraordinary light rays for the Cs_4PbBr_6 crystals are also fitted and the results are shown in Supplementary Fig. 15a. These results confirm that our refractive index measurements are effective and reliable. As shown in Supplementary Fig. 15b, the embedded ordered aligned $CsPbBr_3$ NCs provide a fortuitous wavelength dependence of the refractive index difference between n_o and n_e to compensate the wavelength dependence of the Cs_4PbBr_6 matrix, so that the QW effect of sample II is achromatic.

We further compared the degree of polarization of the 532 nm and 633 nm laser beams for samples I and II at different polarization angles (ϕ), and the results are shown in Fig. 3a,b. The degree of polarization ρ is defined as

$$\rho = \frac{I_{max} - I_{min}}{I_{max} + I_{min}}, \quad (3)$$

where I_{max} and I_{min} are the maximum and minimum intensities of the transmitted light, respectively, after the polarizer when changing the polarization angle of the incident light. Without a sample, the transmitted light is fully linearly polarized with $\rho \approx 1$ (Fig. 3a). For sample I, the value of ρ was slightly affected by the incident angle (ϕ), while a strong modulation of ρ with respect to ϕ was observed for sample II. When the 532 nm laser is replaced by the 633 nm laser, we noticed that ρ has a definite relative variation with respect to wavelength for sample I, but the polarization modulation remains similar as before for sample II. We further measured ρ under incident light from light-emitting diodes of 544, 585, 598, 648, 701, 723 and 799 nm for sample II (see Fig. 3c). The observed achromatic retardation is consistent with theoretical fitting (solid lines).

The phase shift of conventional QW plates between the ordinary and extraordinary rays depends on the wavelength λ

according to $\frac{2\pi}{\lambda}\,|n_e - n_o|\,d$, which leads to dispersion of the wave-plate. From this perspective, the observed unusual retardation of sample II can be explained by matching of the refractive index difference with the wavelength. This phenomenon can also be described as a compensating effect of the embedded $CsPbBr_3$ NCs on the effective refractive index. According to the equations (1) and (2), the achromatic retardation of perovskite Cs_4PbBr_6 crystals should be strongly affected by their thickness. As shown in Supplementary Figs. 16 and 17, the degree of polarization for transmitted light does vary with the thickness of the Cs_4PbBr_6 crystals, as expected.

To illustrate the directional alignment effects of embedded $CsPbBr_3$ NCs in the Cs_4PbBr_6 crystal, we further studied the birefringence properties of other systems that contain randomly distributed NCs, including colloidal $CsPbBr_3$ NCs in toluene (Supplementary Fig. 18), a polystyrene composite film with embedded $MAPbBr_3$ NCs (MA = methylammonium; Supplementary Fig. 19) and a silica monolith with embedded $Cd_xZn_{1-x}Se_yS_{1-y}$ NCs (Supplementary Fig. 20). None of these samples shows polarization modulations. It is worth noting that the NCs are randomly dispersed in toluene, polystyrene and the silica matrix, while the $CsPbBr_3$ NCs embedded in the Cs_4PbBr_6 crystals are directionally well aligned. Therefore, we propose that the structure of the Cs_4PbBr_6 crystals with order-aligned $CsPbBr_3$ NCs produces the observed achromatic retardation effects.

The use of Cs_4PbBr_6 crystals with embedded $CsPbBr_3$ NCs as a QW plate was further investigated by conducting the measurements using different laser intensities. As shown in Supplementary Fig. 21, the QW plate effect of sample II is not obvious when the power density of the incident laser exceeds $40.5\,mW\,cm^{-2}$. This phenomenon can be explained by the laser-induced heating effect, which was also confirmed by polarization modulation measurements at high temperature. As shown in Supplementary Fig. 22, the QW plate effect of sample II becomes weak as the temperature is increased up to $73\,°C$.

In summary, we discovered a remarkable achromatic retardation in the Cs_4PbBr_6 crystal host with embedded $CsPbBr_3$ NCs. The crystal can modulate the polarization of light without any obvious wavelength dependence throughout the range of 532–800 nm, which is an extremely rare optical property according to previous studies of single-component inorganic crystals. Modelling our data using a continuum theory for crystal birefringence suggests that the embedded $CsPbBr_3$ NCs lead to correct dispersion in the birefringence of the Cs_4PbBr_6 crystals. In comparison with multiple-layered systems reported in previous work, the Cs_4PbBr_6 crystals show the great advantages of one-step growth, easy post-processing, stability and having a wide waveband in the visible regime. Moreover, the unique feature of NC-embedded crystals offers structural inspiration for the design of other novel optical materials, such as multi-purpose systems working as a microscopic sensor, a polarization detector as well as a transmissive polarization controller.

Online content

Any methods, additional references, Nature Research reporting summaries, source data, extended data, supplementary information, acknowledgements, peer review information; details of author contributions and competing interests; and statements of data and code availability are available at https://doi.org/10.1038/s41566-021-00865-0.

References

1. Mitchell, S. An achromatic three-quarter wave plate for ultra-violet. *Nature* **212**, 65–66 (1966).
2. Samoylov, A. V., Samoylov, V. S., Vidmachenko, A. P. & Perekhod, A. V. Achromatic and super-achromatic zero-order waveplates. *J. Quant. Spectrosc. Radiat. Transf.* **88**, 319–325 (2004).
3. Roberts, N. W., Chiou, T. H., Marshall, N. J. & Cronin, T. W. A biological quarter-wave retarder with excellent achromaticity in the visible wavelength region. *Nat. Photonics* **3**, 641–644 (2009).
4. Daly, I. M. et al. Dynamic polarization vision in mantis shrimps. *Nat. Commun.* **7**, 12140 (2016).
5. Holt, A. L., Vahidinia, S., Gagnon, Y. L., Morse, D. E. & Sweeney, A. M. Photosymbiotic giant clams are transformers of solar flux. *J. R. Soc. Interface* **11**, 20140678 (2014).
6. Feller, K. D., Jordan, T. M., Wilby, D. & Roberts, N. W. Selection of the intrinsic polarization properties of animal optical materials creates enhanced structural reflectivity and camouflage. *Philos. Trans. R. Soc. Lond. B* **372**, 20160336 (2017).
7. Jacobs, M. et al. Photonic multilayer structure of *Begonia* chloroplasts enhances photosynthetic efficiency. *Nat. Plants* **2**, 16162 (2016).
8. Saha, A., Bhattacharya, K. & Chakraborty, A. K. Achromatic quarter-wave plate using crystalline quartz. *Appl. Opt.* **51**, 1976–1980 (2012).
9. Nagai, M. et al. Achromatic THz wave plate composed of stacked parallel metal plates. *Opt. Lett.* **39**, 146–149 (2014).
10. Nagai, M. et al. Achromatic wave plate in THz frequency region based on parallel metal plate waveguides with a pillar array. *Opt. Express* **23**, 4641–4649 (2015).
11. Karimi, E. et al. Generating optical orbital angular momentum at visible wavelengths using a plasmonic metasurface. *Light Sci. Appl.* **3**, e167 (2014).
12. Smartt, R. N. & Steel, W. H. Birefringence of quartz and calcite. *J. Opt. Soc. Am.* **49**, 710–712 (1959).
13. Beckers, J. M. Achromatic linear retarders. *Appl. Opt.* **10**, 973–975 (1971).
14. Mcintyre, C. M. & Harris, S. E. Achromatic wave plates for visible spectrum. *J. Opt. Soc. Am.* **58**, 1575–1580 (1968).
15. Koester, C. J. Achromatic combinations of half-wave plates. *J. Opt. Soc. Am.* **49**, 405–409 (1959).
16. Boulbry, B., Bousquet, B., Le Jeune, B., Guern, Y. & Lotrian, J. Polarization errors associated with zero-order achromatic quarter-wave plates in the whole visible spectral range. *Opt. Express* **9**, 225–235 (2001).
17. Peng, W. et al. Solution-Grown Monocrystalline hybrid perovskite films for hole-transporter-free solar cells. *Adv. Mater.* **28**, 3383–3390 (2016).
18. Chen, Z. et al. Thin single crystal perovskite solar cells to harvest below-bandgap light absorption. *Nat. Commun.* **8**, 1890 (2017).
19. Cao, Y. et al. Perovskite light-emitting diodes based on spontaneously formed submicrometre-scale structures. *Nature* **562**, 249–253 (2018).
20. Chen, M., Shan, X., Geske, T., Li, J. & Yu, Z. Manipulating ion migration for highly stable light-emitting diodes with single-crystalline organometal halide perovskite microplatelets. *ACS Nano* **11**, 6312–6318 (2017).
21. Hu, X. et al. Direct vapor growth of perovskite $CsPbBr_3$ nanoplate electroluminescence devices. *ACS Nano* **11**, 9869–9876 (2017).
22. Liu, Y. et al. Thinness- and shape-controlled growth for ultrathin single-crystalline perovskite wafers for mass production of superior photoelectronic devices. *Adv. Mater.* **28**, 9204–9209 (2016).
23. Zhang, Q., Ha, S. T., Liu, X., Sum, T. C. & Xiong, Q. Room-temperature near-infrared high-Q perovskite whispering-gallery planar nanolasers. *Nano Lett.* **14**, 5995–6001 (2014).
24. Ye, H. Y. et al. Metal-free three-dimensional perovskite ferroelectrics. *Science* **361**, 151–155 (2018).
25. Chen, X. M. et al. Centimeter-sized Cs_4PbBr_6 crystals with embedded $CsPbBr_3$ nanocrystals showing superior photoluminescence: nonstoichiometry induced transformation and light-emitting applications. *Adv. Funct. Mater.* **28**, 1706567 (2018).
26. Zhang, Z. J. et al. Aqueous solution growth of millimeter-sized nongreen-luminescent wide bandgap Cs_4PbBr_6 bulk crystal. *Cryst. Growth Des.* **18**, 6393–6398 (2018).
27. Møller, C. K. On the structure of caesium hexahalogeno-plumbates (II). *Matemat. Fysis. Meddel.* **32**, 1–27 (1959).
28. Powell, J. A. Refractive-index and birefringence of 2H silicon-carbide. *J. Opt. Soc. Am.* **62**, 341–344 (1972).
29. Walsh, T. E. Birefringence of cadmium sulfide single-crystals. *J. Opt. Soc. Am.* **62**, 81–83 (1972).
30. Kadro, J. M., Nonomura, K., Gachet, D., Gratzel, M. & Hagfeldt, A. Facile route to freestanding $CH_3NH_3PbI_3$ crystals using inverse solubility. *Sci. Rep.* **5**, 11654 (2015).
31. Tan, J. C., Saines, P. J., Bithell, E. G. & Cheetham, A. K. Hybrid nanosheets of an inorganic–organic framework material: facile synthesis, structure, and elastic properties. *ACS Nano* **6**, 615–621 (2012).
32. Olivares, J. & Cabrera, J. M. Guided modes with ordinary refractive-index in proton-exchanged $LiNbO_3$ wave-guides. *Appl. Phys. Lett.* **62**, 2468–2470 (1993).
33. Smith, D. S., Riccius, H. D. & Edwin, R. P. Refractive-indexes of lithium-niobate. *Opt. Commun.* **17**, 332–335 (1976).

Methods

Preparation of pure Cs$_4$PbBr$_6$ crystals. Pure Cs$_4$PbBr$_6$ crystals were prepared by adapting a reported procedure[26]. Caesium bromide (CsBr; 235 mmol, 50 g; Aladdin, 99.9%) was dissolved in deionized water (50 ml) at 90 °C and a nearly saturated concentrated CsBr aqueous solution was obtained. Then the solution was kept at this temperature for 2 hours. After that, a fixed amount of lead(II) bromide (PbBr$_2$; 1.35 mmol, 0.5 g; Aladdin, 99%) was dissolved in concentrated hydrobromic acid (HBr; 5 ml; Aladdin, 48 wt% in water). The PbBr$_2$ solution was added dropwise to the CsBr solution with vigorous stirring at 90 °C until a transparent solution was obtained. The solution was kept at 90 °C for 2 hours before being cooled to room temperature at a rate of 2 °C h^{-1}. Finally, pure Cs$_4$PbBr$_6$ single crystals with a lateral size of 3 mm were obtained.

Preparation of Cs$_4$PbBr$_6$ crystals with embedded CsPbBr$_3$ nanocrystals. Cs$_4$PbBr$_6$ single crystals with embedded CsPbBr$_3$ NCs were grown using a slow-cooling method[25]. In a flask, PbBr$_2$ (2.5 mmol, 0.917 g) and CsBr (10 mmol, 2.130 g) were dissolved in a 50 ml mixture of dimethylformamide (DMF; Beijing Chemical Reagent, analytical grade) and HBr (volume ratio 5:4) at room temperature. The temperature of the crystal growth was controlled using an external water bath, with an accuracy of ±0.01 °C. The solution was first heated to 80 °C and then cooled to room temperature. Single crystals were formed at the bottom of the flask. These crystals were washed using γ-butyrolactone (Beijing Chemical Reagent, analytical grade) and toluene (Beijing Chemical Reagent, analytical grade).

Preparation of CsPbBr$_3$ nanocrystals. A fixed amount of CsBr and the PbBr$_2$ were mixed in DMF, then the mixture was dried at 50 °C to obtain CsPbBr$_3$ as an orange powder. Colloidal NCs were fabricated following the reported ligand-assisted reprecipitation technique[34]. A certain amount of CsPbBr$_3$ powder (0.5 mmol, 0.290 g) was dissolved in DMF (5 ml) with *n*-octylamine (20 µl; Aladdin, ≥99%) and oleic acid (0.5 ml) to form a precursor solution. Then the precursor solution (200 µl) was added dropwise to toluene (10 ml) with vigorous stirring, and the yellow-green colloidal NC solution was obtained.

Preparation of colloidal MAPbBr$_3$ nanocrystals. Methylammonium bromide (2 mmol, 0.179 g; Aladdin, 33 wt% in absolute ethanol) and HBr were dissolved in DMF (3 ml), and this was labelled as solution 1. PbBr$_2$ (2 mmol, 0.734 g) was dissolved in DMF (5 ml), and this was labelled as solution 2. Oleic acid (5 ml; Alfa Aesar, ≥90%), *n*-octylamine (0.2 ml) and *n*-hexane (100 ml; TGchem, analytical grade) were mixed, and and this was labelled as solution 3. Solution 1 and solution 2 were added dropwise to solution 3 under vigorous stirring until a white emulsion solution was obtained. Then, acetone (80 ml; TGchem, analytical grade) was added to the emulsion solution as a demulsifier to initiate the demulsion process. The solution was centrifuged at 7,000 revolutions per minute (r.p.m.) for 3 min to obtain a yellow-green precipitate. The precipitate was re-dissolved in *n*-hexane (10 ml) and centrifuged at 7,000 rpm for 3 min; he supernatant was dissolved in *n*-hexane to obtain a solution of green MAPbBr$_3$ colloidal NCs. Finally, the concentrated MAPbBr$_3$ NC solution with slight *n*-hexane was obtained through rotary evaporation.

Preparation of MAPbBr$_3$ nanocrystals in a polystyrene composite film. Concentrated MAPbBr$_3$ NC colloidal solution (300 µl) and polystyrene (20 g; J&K Scientific, molecular weight 100,000) were dissolved in dichloromethane (50 ml; TGchem, analytical grade) and stirred for 24 hours to obtain a viscous solution, which was then poured into a mould. After three days, the polystyrene composite containing MAPbBr$_3$ NCs was formed.

Preparation of Cd$_x$Zn$_{1-x}$Se$_y$S$_{1-y}$ nanocrystals in a silica monolith. Tetraethylorthosilicate (Aladdin, 98%) was chosen as the silica precursor. First, mercaptohexanol-capped Cd$_x$Zn$_{1-x}$Se$_y$S$_{1-y}$ NCs (460 µl, 25 mg ml^{-1}) were added to a beaker; then, 3-mercaptopropyltrimethoxysilane (200 µl; Aladdin, 97%) was added to the beaker. (3-Aminopropyl)triethoxysilane (Aladdin, 98%) was used to initiate the gelling process. Finally, the gels were transferred into moulds to form the quantum dot–silica monolith.

Structure characterization. The Cs$_4$PbBr$_6$ crystals used in this work with and without embedded CsPbBr$_3$ NCs are 1.1–1.3 mm thick. The thickness-measurement image is shown in Supplementary Fig. 1, and the thickness of the simples was characterized using a thickness gauge (Syntek). The crystal phases of the two samples were characterized via X-ray diffraction. The X-ray diffraction measurements were conducted using a Bruker/D8 FOCUS X-ray diffractometer, using a Cu Kα radiation source (wavelength at 1.5405 Å). The Cs$_4$PbBr$_6$ crystal with and without embedded CsPbBr$_3$ NCs was further confirmed by the Tyndall effect and HRTEM analysis, where the Tyndall effect was determined using a 633 nm laser-integrated Olympus BX51 M microscope. The crystal slice obtained via focused ion beam milling for HRTEM measurements was fabricated as follows: a surface protective layer was first deposited using an electron beam and the gallium-ion beam of an SMI3200SE system; the sample was cut using the gallium-ion beam of the SMI3200SE, and was then transferred to an FB-2000A instrument. Using the FB-2000A, a small block sample with a size of tens of micrometres was fixed on a TEM mesh and reduced to approximately 100 nm under cryogenic conditions (−140 °C) using the gallium-ion beam of a Helios G4 CX microscope. The HRTEM observations were recorded using a JEM-F200 (JEOL) TEM instrument operating at an accelerating voltage of 200 kV.

Optical property characterization. The photoluminescence spectra were obtained using a fluorescence spectrometer (F-380, Tianjin Gangdong Technology). UV-visible diffuse reflection spectra were measured using a spectrophotometer (TU-1901, Persee).

Polarization modulation measurements. Various light sources were applied to measure the light modulation effects of single crystals, including a 532 nm laser (GT1+11A, Viasho Technology), a 633 nm laser (DH-HN helium laser, Daheng Optics) and a xenon lamp (7IPX5002, Sofn Instruments). The long-pass filter, aperture, attenuator, polarizer and lens were obtained from Daheng Optics. For details of the test, see the description following the legend of the resulting figure.

Data availability
Source data are provided with this paper. All other data that support the plots within this paper and other findings of this study are available from the corresponding authors upon reasonable request.

References

34. Zhang, F. et al. Brightly luminescent and color-tunable colloidal CH$_3$NH$_3$PbX$_3$ (X = Br, I, Cl) quantum dots: potential alternatives for display technology. *ACS Nano* **9**, 4533–4542 (2015).

Acknowledgements

Author contributions

H.Z. conceived and supervised the project. X.C., W.-g.L. and J.T. fabricated the materials. X.C., W.-g.L. and Y.W. carried out the spectroscopic measurements. Y.Z. proposed the theoretical model and performed the fitting. H.Z., G.D.S., X.C., Y.W. and Y.Z. wrote the manuscript with contribution from all the authors.

Competing interests
The authors declare no competing interests.

Additional information